Gamma Measurements with the 4π BaF_2 Detector Array for the FRANZ Facility

Stefan Schmidt

Contents

FRANZ refers to the German abbreviation for the
Frankfurt Neutron Source at the Stern-Gerlach-Zentrum.

1 Introduction

The 4π detector investigated in this thesis is used for the measurement of neutron capture cross-sections. Values obtained with higher accuracy by creating unprecedented neutron fluxes in a laboratory environment will allow further tests of the currently favoured theories about the stellar s-process (for "*s*low neutron capture process") – a stage in stellar evolution of heavy element nucleosynthesis.

s-process

As described in [19, p. 297], towards the end of their lifetime on the main sequence, i.e. when most of the central hydrogen has been burnt to helium, stars move along the giant branch in the Hertzsprung-Russell diagram. Sustaining their temperature, the stars' luminosity increases and their central electrons enter a state of degeneration, in which the pressure is independent of the temperature (unlike the ideal gas). Due to the onset of helium burning, the core heats up until the degeneration suddenly stops. Then, the pressure builds up rapidly resulting in the so-called "helium flash" at the upper end of the giant branch. This explosion does not destroy the star, instead it is the beginning of the central helium burning.

Once the helium is burnt, the luminosity increases a second time and the star finally reaches the asymptotic giant branch. Inside the star, which has by now become a red giant, α reactions create nuclei that provide excess neutrons for subsequent capture events (cf. [3, p. 179]). Typical temperatures of the surrounding plasma are around 200–300 million Kelvin (corresponding to a thermal energy of 25 keV; see [4, p. 189]).

Lacking an electric charge, neutrons are captured by the predominant iron (and similar elements) on a timescale of months or years while the β decay time is significantly shorter [3, p. 179]. Due to these long capture times, this process is called "s-process".

Astronomical clocks

In order to estimate the age of the universe, "astronomical clocks" are required. Currently, the standard way to approximate the age is based on the Hubble parameter that describes the expansion of the universe. However, this approach suffers from a problem:

Most importantly, nowadays the Hubble parameter is not considered a constant anymore – current models assume that its value actually changes due to the accelerated expansion of the universe. Therefore, an in-depth understanding of the cosmological expansion is necessary in order to get accurate results. Due to improved methods of observation and analysis, current measurements of H_0 are very reliable [7], but older data have been affected by large uncertainties yielding re-

sults ranging from 2 (with $t = \frac{1}{H_0}$ and $H_0 = 500\,\frac{\mathrm{km\,sec}}{\mathrm{Mpc}}$, cf. [10]) to 40 billion years ($H_0 = 24\,\frac{\mathrm{km\,sec}}{\mathrm{Mpc}}$, cf. [13]).

Theoretical models that employ the neutron capture cross-section to estimate the age of the universe do not suffer from these problems. They may provide a way to check the results obtained through the aforementioned observations by simulating the development of different initial sets of isotopic abundances. Each of these sets should result in a certain set of abundances of heavy nuclei that depends on the period examined. Ultimately, a model that reproduces the abundances measured today should then yield the correct age of the universe.

Accelerator-driven systems

Furthermore, the exact knowledge of neutron capture cross-sections is required for the design of nuclear reactors as well as accelerator-driven systems (ADS). The latter utilises a proton beam hitting a specially designed target to generate spallation neutrons, which in turn drive a sub-critical core [11]. While the net output is obviously lower than that of a contemporary reactor due to the power consumption of the accelerator, the setup is highly controllable: If an emergency shutdown is required, it is only necessary to turn off the proton beam and spallation neutron production stops immediately – current reactors need to wait for control rods to become sub-critical. For either implementation (ADS or nuclear reactor), even small cross-section uncertainties can have a large impact on reactor design. For example, if calculations for the reactor volume are based on flawed cross-section data, the number of reactions within a given time might be insufficient to achieve the desired power output.

These systems are currently also explored as a way of transforming long-lived radioactive waste into short-lived isotopes thereby reducing the problems of final storage of nuclear waste.

Other intense neutron facilities

Today, several other high energy neutron sources exist all over the world. However, none of these allows to produce a spectrum of 1–200 keV neutrons with a flux as high as $10^7\,\frac{1}{\mathrm{cm^2 sec}}$, three orders of magnitude beyond the value reached at the Karlsruhe Van de Graaff accelerator.

Large flight paths – the CERN n_TOF experiment for neutron fluxes of $5 \cdot 10^4\,\frac{1}{\mathrm{cm^2 sec}}$ uses a distance of 183 m [2] – do not allow easy discrimination between true capture events and background events due to scattered neutrons captured inside the scintillator [20, p. 600]. In Karlsruhe, where preceding experiments in the neutron energy range from 1–200 keV were conducted, the primary neutron flight path was 80 cm. The distance from the sample to the 4π detector array was 10 cm. Neutrons scattered by the sample under investigation travel the latter distance which is of the

same order of magnitude as the primary flight path. Therefore, the time of flight spectra will show an interval that is free of neutron captures in the scintillator.

Among others, the n_TOF experiment mentioned above tries to examine neutron capture cross-sections, for example to evaluate ADS designs or different theories of stellar nucleosynthesis [8, 14]. Due to the better resolution and extended range in neutron energy, the n_TOF results will complement the measurements planned at Frankfurt, which in turn will benefit from the much higher flux.

2 Setup and relevant processes

2.1 Possible measurements

Similar to the setup in Karlsruhe (cf. Fig. 1), a proton beam is shot at a lithium target (subsequently referred to as *target*), thereby creating neutrons in a ^{7}Li(p,n)^{7}Be reaction. A summary of [15, p. 7–8] describes the two different approaches to measuring the capture cross-sections:

2.1.1 Time of flight measurements

The γ flash from the ^{7}Li(p,n)^{7}Be reaction (red peak in Fig. 1) is used to trigger the start of the time of flight measurement. Depending on their energy, the neutrons take some time to transit the path to the sample and be captured there. The green bump in Fig. 1 results from the γ quanta emitted in the capture event. The number of photons emitted in this process ("multiplicity") varies, depending on the number of de-excitation states passed, so proper detection of a capture event usually requires correctly determining the sum energy as an important signature of such an event. After that, secondary processes dominate the pulse-height spectrum. Since the sample is exposed to a multitude of different neutron energies, it is possible to calculate the differential cross-section $\frac{\mathrm{d}\sigma}{\mathrm{d}E}$.

2.1.2 Activation measurements

In comparison to the time of flight measurements, in activation measurements the flight path of the neutrons is not constrained to 0° because no collimator is used. In this case, the neutron energy distribution integrated over the full solid angle is similar to the stellar neutron distribution (see Fig. 2). This is favourable as the obtained cross-section data only needs minor corrections when used for s-process models. After being exposed to the neutron beam for a certain time, the sample is removed from the beam and its activity is measured. While this method is significantly more sensitive than the time of flight method (see [15, p. 8]), the resultant value only

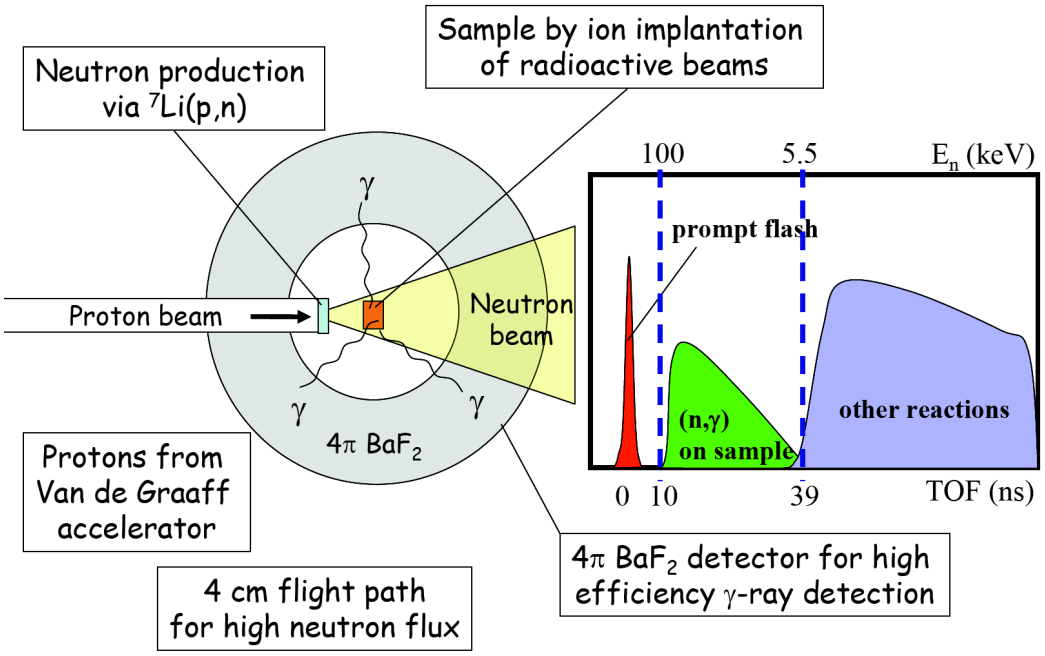

Figure 1: Overview over the experimental setup together with an exemplary pulse-height spectrum recorded in time of flight measurements (see [9, 16]).

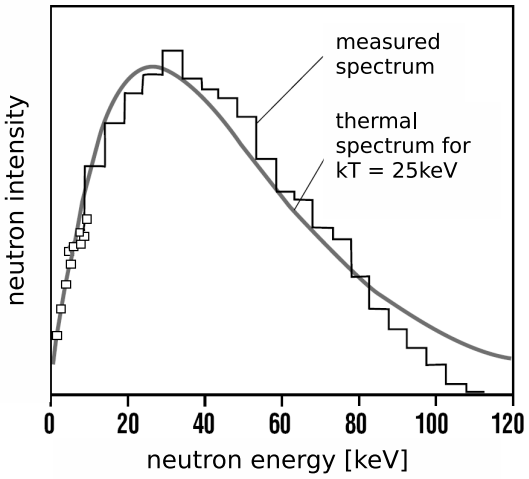

Figure 2: Lab approximation of stellar neutron distribution in activation measurements (taken from [4, p. 191]).

allows the determination of the convolution of the differential cross-section with the activation spectrum, but not of the differential cross-section itself.

2.2 Array setup

One possible signature of a capture event is the sum energy of all photons, so it is important to detect all of them. Therefore, this detector covers the full solid angle using a honeycomb frame that consists of 42 positions. Of these, 38 contain regular detector modules that essentially consist of a scintillator crystal made from BaF_2, and a photomultiplier tube. In order to operate the latter, a voltage divider is plugged into the rear end of each segment. Two more slots are occupied by special modules containing a slit for the sample changer. These are the polar segments set up perpendicularly to the beam axis (modules 8 and 13). Module 42 is positioned along the beam axis; it employs a crystal with a centre hole to allow the beam to exit the detector array. The final slot, no 1, contains just the lead collimator that leaves only a small opening for the neutron beam. As a reference, Fig. 3 is given to illustrate the mounting of a module in the honeycomb structure.

2.2.1 BaF_2 crystal

Each BaF_2 crystal is shaped like a frustum ("Pyramidenstumpf" in German), with the base shaped either pentagonally or hexagonally in order to approximate a sphere with the sample at its centre. Despite the different shapes, all modules cover the

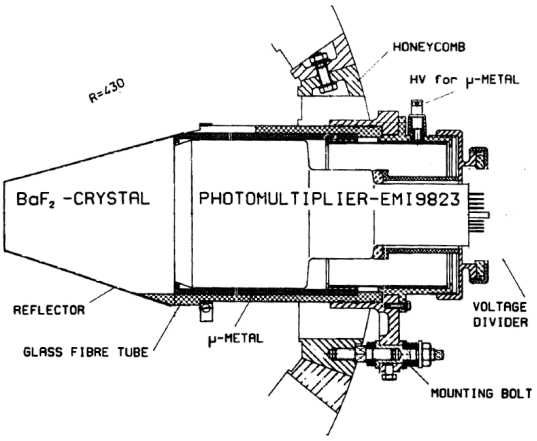

Figure 3: Module setup (taken from [20, p. 602]).

same solid angle. This simplifies the analysis of the results since weighting the data from the different modules is not necessary. According to [20, p. 599], at the time the array was built in the 1980s, BaF_2 had the best properties for the detection of 6–8 MeV photons. As a scintillator, it provides the opportunity for time measurements with sub-nanosecond resolution while also allowing energy measurements with sufficiently good resolution. Moreover, it is not as sensitive to neutrons scattered by the sample as, for example, BGO (see below).

Each photon resulting from a capture event releases very few scintillation photons. Therefore, it is imperative to allow photons to leave the crystal only through the photomultiplier. This is ensured by several layers of PTFE tape wrapped around the scintillator. While fairly harmless in its present crystalline form, the crystal is covered by another two layers, one of aluminium foil and one of black tape, to protect anyone handling the detector from the potentially poisonous [20, p. 604] fluoride component.

BaF_2 as detector material

Summarising [20, pp. 598–599], only a handful of materials needed to be considered as a γ detector due to the required crystal size: NaI(Tl), BGO, CsI(Tl) and BaF_2. Because of the high neutron capture cross-section of the only naturally abundant isotope of iodine, ^{127}I, of 635 mb at 30 keV (just within the energy range the detector should operate), scintillators containing iodine could not be used. Neutrons scattered by the sample instead of being captured would react within the scintillator and create a considerable background.

In comparison to BGO, BaF_2 has several favourable properties. Firstly, the fast component decays in less than a nanosecond [12, p. 110], while in $Bi_4Ge_3O_{12}$ the only

existent component decays in 350 ns. Since a fast response is important, it is not immediately obvious why an anorganic scintillator was used: Organic scintillators have a low atomic number Z but the response probability increases with Z^2, so in order to obtain similar properties, an organic scintillator of around 2 m would be necessary.

Secondly, the neutron capture cross section of ^{138}Ba, the most abundant barium isotope (almost 72 %, see [6, p. 54]), is rather low.

Unfortunately barium and radium are chemically homologous, so α radiation due to Ra impurities within the crystals is unavoidable, thus creating a time-independent background [20, pp. 599]. But since the α-induced signals from radium exhibit a different pulse shape, they can easily be discriminated.

2.2.2 Photomultiplier tube

The photomultiplier tube (PMT) is optically coupled to the scintillator using silicon oil. This connection is necessitated by the difference between the refraction indices of BaF_2 and the surface of the PMT. Without connection the probability of photon reflection at the interface between the two media would increase, thus degrading the signal.

Inside the tube, the photoelectric effect causes electrons to be emitted from the tube's photocathode. Subsequently, they are accelerated towards the different dynodes where they produce a readout signal (for a more detailed description see 2.4). The appropriate operating voltage depends on the module, ranging from slightly below 2 000 V to 2 400 V; the typical current of about 1.6 mA leads to approximately 4 W per module. The voltage for the dynodes is supplied by a resistor chain within a voltage divider which is simply plugged into the rear end of the module. It provides controls for modifying the voltage of the focussing electrode (labelled "F", see Fig. 4) and the second dynode ("D2") – fine-tuning these settings may help to increase the pulse height output of the module.

Negative charges accelerated within the PMT are subject to the Lorentz force. Therefore, it is necessary to shield the setup from magnetic fields. This is achieved by wrapping the tube in three layers of μ-metal, a material with a very high relative permeability. Electric shielding of the PMT interior can be improved by connecting these layers to the photocathode potential, thus preventing the negative charges from interacting with the tube walls.

2.2.3 Automated sample changer

When the proton beam is turned on, the area around the detector must temporarily be declared as radiation area without direct access. Therefore, samples should only be changed online using the sample changer attached to the frame. It cycles to the

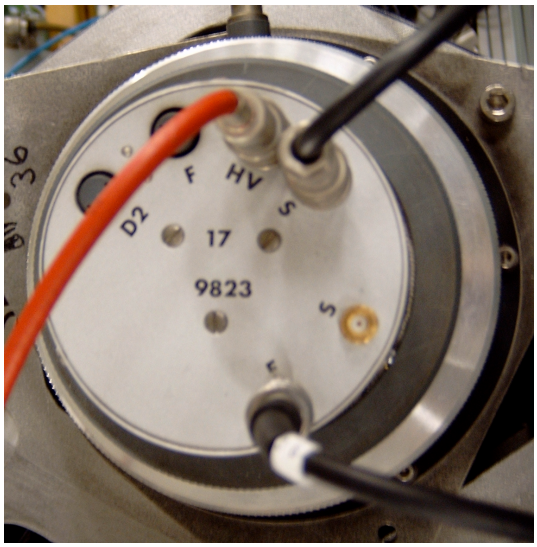

Figure 4: Voltage divider plugged into the end of a module; the connectors for high-voltage (HV), shielding (S, adjacent to HV), fast and slow signal (F and S, bottom right), as well as the adjusters for the focussing (F, next to D2) and the second dynode (D2) are clearly visible.

next sample position once a certain amount of charge has been deposited on the neutron target. As was said in [20, p. 614], this may cause errors if the amount of neutrons per proton decreases over time.

More importantly, however, it provides a means to determine backgrounds, for example from the concrete of the building. It is recommended [20, p. 613] that at least four of the changer's eight positions be occupied according to a common pattern:

1. of course, the sample in question,
2. a reference sample, usually gold the capture cross-section of which is very well known,
3. a carbon sample with negligible capture cross-section that allows the measurement of the background which results from neutrons scattered by the sample and captured in or near the BaF_2 modules,
4. an empty sample to measure the background due to natural radioactivity.

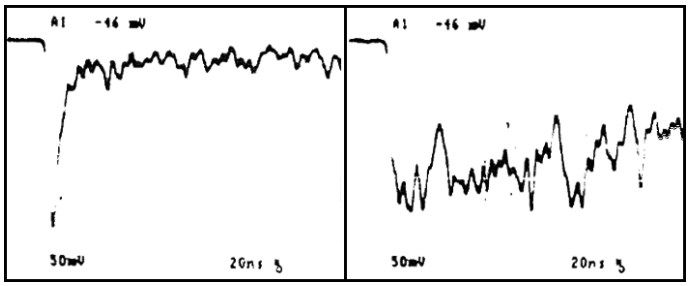

Figure 5: Comparison [20, p. 605] of a γ ray from 662 keV (^{60}Co source, left) and a 7.7 MeV α particle (right). The picture is a photograph from an oscilloscope with time and voltage plotted in x and y direction respectively.

Sources for background

If neutrons are scattered by the sample, they may interact with several other components of the experiment. They might be captured in the scintillator and release a photon cascade there – with BaF_2 as detector material, this is not too problematic because the sum energy of such events differs from events in the sample. Furthermore, scattered neutrons may react with the shielding around the neutron production target, thereby causing additional undesired background. To compensate for this effect, the current setup employs an automated sample changer that is recommended to contain a sample of carbon: the capture cross-section of this element is negligible, so any spectrum recorded with this sample should be considered as caused by neutron scattering – the measured background can therefore be subtracted from measurements with the sample in question. This also helps reducing the background caused by interactions of scattered neutrons with air; further improvements may be achieved by using an evacuated flight tube, as was already suggested at the time the detector was built (cf. [20, p. 617]).

2.2.4 Analysis software

The quality of the acquired data was improved further by using a minimum energy threshold. Comparing the signal from a 662 keV γ and from a 7.7 MeV α particle (see Fig. 5), the most important difference is that a signal created by the α radiation does not exhibit a "fast component". This name refers to the fast scintillation response yielding a sharp peak (left panel). The energy of a particle essentially corresponds to the area between the signal and the base line. As α signals exhibit an amplitude much lower than the fast component caused by γ quanta, they can, therefore, be discriminated easily. This can be achieved by analysing the ratio of the fast component to the slow component.

Since the energy of the 662 keV photons is far below the expected energy range (6-8 MeV), it is safe to use a peak threshold of about 700 keV below which any events are discarded (cf. [20, p. 607]).

2.3 Semi-conducting γ detector systems

Instead of using a scintillation process, another common way to detect γ photons involves the band gap in semi-conductors. These devices work similar to ionisation chambers in which incident radiation creates electron-ion pairs. By applying an electrical field, the charge carriers are driven towards the electrodes resulting in a voltage pulse.

2.3.1 Semi-conductors

In comparison to single atoms, the energy difference in solids between different electron energy levels is extremely small. In other words, there are regions in which (nearly) every electron energy is "allowed". These zones are called "bands", they are separated by "band gaps" where there are no allowed electron states.

The position of the Fermi level – the energy of the highest occupied electron state at $T = 0$ – relative to band gaps defines the type of solid: if the Fermi level is inside a band of allowed electron states, the solid is called a metal. If it is outside of such a band, so within a band gap, the solid may either be a semi-conductor or an insulator depending on the size of the gap – with semi-conductors exhibiting a gap of the order of electron volts while insulators have much bigger gaps. Only for the latter two types, the definition of valence and conduction band is possible: the latter is the lowest unoccupied (perfectly true only at $T = 0$) band, while the former refers to the highest occupied band at $T = 0$.

The requirement of a small band gap for semi-conducting behaviour leads to only a small number of possible materials with silicon and germanium being the most common. By highly controlled impurification of a silicon monocrystal with other materials of the order of particles per million – the process is called doping – the major charge carrier type may be changed. If the doping leads to electrons being the important component for transporting a current through the solid, it is called an n-type semi-conductor ("n" for negative). Otherwise, if holes are the primary charge carrier – in other words conduction primarily takes place in the valence and not in the conduction band (as it does for electrons) – the solid is called a p-type semi-conductor ("p" for positive).

p-n diodes and p-i-n diodes

By bringing p-type and n-type semi-conductors into very close contact, a p-n junction is created. Without any voltage applied, negative and positive charge carriers

in the vicinity of the junciton diffuse into the other silicium type and recombine with their counterparts. The ions remain in their original position resulting in a so called "space charge region". In this zone, which is also called depleted since there are no free charge carriers, an electrical field points from the p-type to the n-type semi-conductor. Therefore, an electrical current can only pass in conformance with this field, so semi-conductors can be used as diodes. By applying a positive voltage to the n-type and a negative voltage to the p-type ("reverse-biased voltage"), the respective charge carriers are figuratively dragged away from the depleted zone, thus effectively widening the region.

In order to widen the zone even further, another near-intrinsic semi-condcuting layer may be inserted between the p-type and the n-type semi-conductor. Usually, the reverse-biased voltage is then chosen in such a way that the intrinsic zone is entirely depleted.

2.3.2 Semi-conductors as detectors

According to [12, p. 58], an incident photon, which passes through the space charge region – the sensitive volume of a semi-conductor detector – excites electrons along its track pushing them from the valence band to the conduction band, so holes remain in the valence band. Next, the electrons de-excite by creating further electron-hole pairs and phonons (lattice oscillations). Therefore, a trace of highly concentrated charge carriers remains along the track. By collecting the electrons at the anode prior to their recombination the energy loss of the initial photon due to ionisation can be measured.

Comparison of a Si detector and the BaF_2 detector

The major advantage of semi-conductors is the very small band gap of only a few electron volts. This results in a very high relative energy resolution which can be calculated [12, p. 61] by

$$\frac{\sigma(E)}{E_0} = \sqrt{\frac{F \cdot W_i}{E_0}}$$

where F denotes the number of electron-hole pairs multiplied by the so-called Fano factor. This factor stems from the fact that the behaviour of the important semi-conductors (Si) is usually better than the expectation from elementary statistics. For silicon, this factor ranges from approximately 0.09 to 0.14 (cf. [12, p. 61]). W_i refers to the energy required to produce an electron-hole pair – 3.6 eV for silicon. However, it has to be noted that the results from the formula above have never been as good when evaluated experimentally, yet theory and experiment agree on the order of magnitude.

For $E_0 = 0.662\,\mathrm{MeV}$ as well as for $E_0 = 6.1\,\mathrm{MeV}$, the relative resolution is $\approx 10^{-4}$. However, the values obtained for the setup at hand are in the percent region (see Fig. 24 for details), so these different approaches differ by two orders of magnitude.

While having an acceptable energy resolution, the more important property of a scintillator is its very high time resolution. According to [12, p. 110], the fast component of the BaF_2 scintillation light decays in less than a nanosecond while the collection time for electrons in semi-conductor detectors is around 2 ns (see [12, p. 59]).

2.4 Using this setup as a detector

The identification of a neutron capture event requires to measure the γ quanta that are emitted in such events. A single quantum might escape through the space between the crystals or through the unoccupied honeycomb positions. These add to approximately 5 % of the solid angle left uncovered with detectors – the space between the crystals is diffcult to calculate, yet it should be neglectable as a metal sheet of 0.1 mm thickness was used to avoid touching modules.

In most cases, however, a quantum does not escape through one of the slits. Instead, it will most likely interact with a scintillator crystal by transfering its energy to an electron, which then escapes from the atom. The massless photon makes the mass-afflicted electron move; therefore, the nucleus has to move, too, in order for the centre of mass movement (CM system consisting of the negative charge and the ion) to be conserved. According to [18, p. 90], this is the reason why preferably K-shell electrons are emitted. After the negative charge has left the atom, electrons from higher shells fill up the hole while emitting photons the energy of which corresponds to the difference in the binding energy between the former and the current state. These photoelectrons (resulting from the photoelectric effect) constitute the primary contribution to the scintillation pulse.

Unfortunately, not many photons are emitted in the last step (cf. [18, p. 238]), so this signal is converted into a voltage pulse by a sensitive PMT which is optically coupled to the BaF_2 crystal by silicon oil. In the tube, the incident photons interact with the photocathode and electrons are emitted. The latter are then attracted by "dynodes" (gradually less negative plates within the PMT) which are coated with a material like Cs-Sb that tends to emit multiple electrons for each incoming charge [18, p. 241]. Therefore, a single photoelectron creates an avalanche of secondary negative charges that is finally measured by the readout electronics and observed in the energy spectrum as the photopeak.

Beside the primary photoelectric interaction in the scintillator, Compton scattering and pair-production processes take place as well (see also [18, pp. 89-97]). In Compton interactions an electron in an outer atom shell is hit by an incident photon

and both interaction partners are scattered. The photon transfers part of its energy to the electron; however, due to the correlation between the scattering angle of the photon and its energy loss, there is a maximum energy $E_{\mathrm{e,max}}$ the electron can get from the interaction. This energy can easily be calculated using the well-known formula for the Compton effect

$$\Delta\lambda = \lambda' - \lambda = \frac{h}{m_e c^2}(1 - \cos\theta)$$

Employing $E = h \cdot \frac{c}{\lambda}$, the photon energy after the scattering can be obtained using

$$E' = \frac{E m_e c^2}{m_e c^2 + E(1 - \cos\theta)}$$

Therefore, $E_{\mathrm{e,max}}$ is

$$\begin{aligned} E_{\mathrm{e,max}} &= E - E'_{\mathrm{max}} \\ &= E - \left[\frac{E m_e c^2}{m_e c^2 + E(1 - \cos\theta)}\right]_{\mathrm{min}} \\ &= E - \frac{E m_e c^2}{m_e c^2 + 2E} \qquad (\text{with } \theta = \pi) \\ &= \frac{2E}{m_e c^2 + 2E} \end{aligned}$$

which results in the spectrum in a feature called “Compton edge”: This is the maximum energy an electron can get due to Compton scattering. If the outgoing photon is also detected in a scintillator, it is responsible for the “backscatter peak” (because of $\theta = 180°$) corresponding to the minimum photon energy in Compton interaction.

The last process, pair production, is increasingly important for higher energies beyond 1.022 MeV. An incoming photon splits up into an electron-positron pair (again, a mass-afflicted particle like the nucleus is required for momentum conservation, see above). The anti-particle almost immediately annihilates with a negative charge in the area creating two 0.511 MeV photons that can be detected. The other electron may take part in Compton or photoelectric interactions as described above.

2.5 Determination of cross-sections

The detector usually measures the capture cross-section in relation to gold. Therfore, a gold sample is recommended to occupy one of the sample changer’s position (see section 2.2.3). The changer switches the positions once a certain proton charge has been shot at the target, so the target was exposed to a definite integrated neutron flux (supposing that the neutron yield does not decrease over time).

Information from the other samples in the changer can be used to correct the spectra for sample independent neutrons and neutrons captured by BaF_2 (compare [20, p. 614]; for possible background sources, see section 2.2.3).

Depending on the measurement method (activation or time of flight, see section 2.1), different cross-section data can be obtained. In time of flight measurements, it is possible to determine $\frac{d\sigma}{dE}$ because of the different neutron energies, while activation measurements only allow the extrapolation of the convolution of the differential cross-section with the activation spectrum.

3 Rebuilding the detector

3.1 Disassembling the detector in Karlsruhe

In Karlsruhe, the single detector modules had to be unmounted, as the transfer to Frankfurt necessearily entailed vibrations that would have damaged the crystals had they remained in the frame. In order to ease unmounting and safely wrapping the modules for transport, the voltage dividers were removed. To unmount the crystals from the frame, it proved to be best to have one person pull the module from the outside while another person ensures from the inside of the support structure that neighbouring crystals are not pushed too close together which could have possibly damaged them. When problems arose while trying to pull out the crystal, a tool ("pull-off tool", "Abzieher" in German) was used successfully.

Due to the fragility of the crystals and the PMTs, only a single layer of two moduleswas stored inside each box, the remaining space was filled with padding material. Because of the modules' brittleness, avoiding any stacking inside each box as well as of the boxes themselves was very important. Therefore, all of the cardbord containers were put on the floor of the cargo area of the transporter.

3.2 Reassembling the detector in Frankfurt

When the frame arrived in Frankfurt, it became obvious that the height of the detector's centre was lower than the beam line of the accelerator, which is at 1.75 m. Therefore, a table was built permanently lifting the frame by almost 75 cm.

Reinstalling the modules proved not to be too difficult – however, a small gap between them had to be maintained allowing possible thermal expansion without the risk of breaking the BaF_2 crystals. For this purpose, a 0.1 mm thick metal sheet was temporarily inserted into the gap between the crystals to check that the distance was acceptable. Since every module has a number corresponding to the number written on the honeycomb structure of the frame, the correct location of the modules was easily determined. One exception were the polar segments where

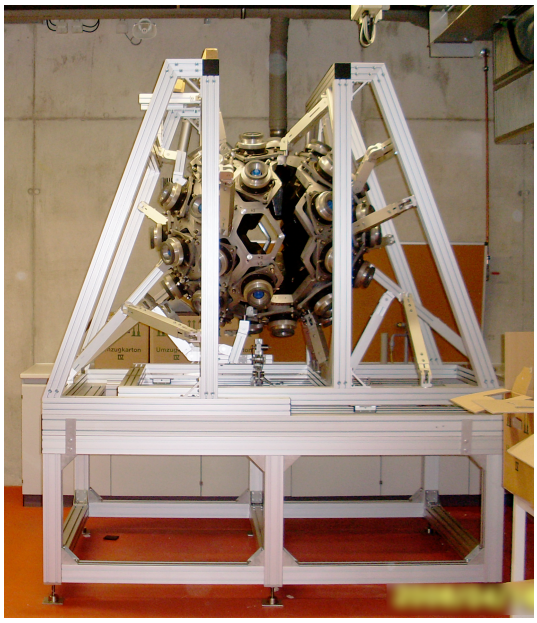

Figure 6: Detector sphere on the support table, most modules (exception: beam entrance and exit segments) are remounted.

there are two numbers given on the frame, one in brackets, which had to be ignored (apparently, a production mistake of the frame), and another one corresponding to the number of the correct module. In Fig. 6 the detector is shown with most modules in place.

When reconnecting the shielding cables, the connector plugs were checked to be fixed tightly in their position. On two modules, the plugs had to be re-glued into their correct positions. In module 34, the shielding connector has been lost during the transfer from Karslruhe.

After mounting the modules, it became obvious that the frame could not be closed completely as one hemisphere had shifted, perhaps during the move from Karlsruhe. However, since the detector had not been tested for over a year and it was not crucial for initial tests to close the sphere, the frame was not readjusted. This was agreed upon considering that during storage or while moving the array to its final position, the hemispheres might shift again.

4 Measurements

With all modules in place, first tests of the spectrum analysis software were conducted using a ^{60}Co source. It was put in the centre of the detector array and a few

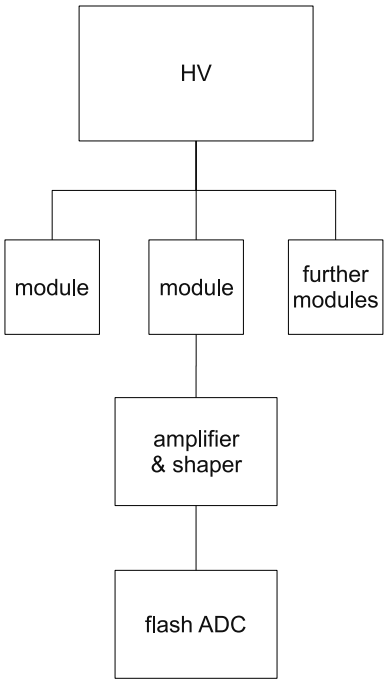

Figure 7: Scheme of the measurement devices for energy calibration. The HV unit supplies voltage to the photomultiplier which is part of a module. The multiplier outputs a capture event signal which is shaped and amplified and finally measured by the flash ADC. For time resolution measurements no amplifier was used.

(almost) randomly selected modules were connected to the analysis computer. This procedure gave a first impression of what the energy spectrum should look like and roughly what the energy resolution would be while proving at the same time that the modules involved had been put in operation successfully.

A simple scheme of the setup used for the following measurements is given in Fig. 7. In order to operate, the photomultipliers were connected to a high-voltage power supply. The module under investigation was connected to the flash ADC, either with the help of a signal amplifier (gain set to 50), that also shapes the signal with a shaping time of (3 μs) in energy resolution measurements or without such a device in time resolution measurements.

4.1 Mollweide projection

There are several approaches to projecting the surface of a sphere in two dimensions [17], for example the Robinson projection or the Hammer projection. Such map

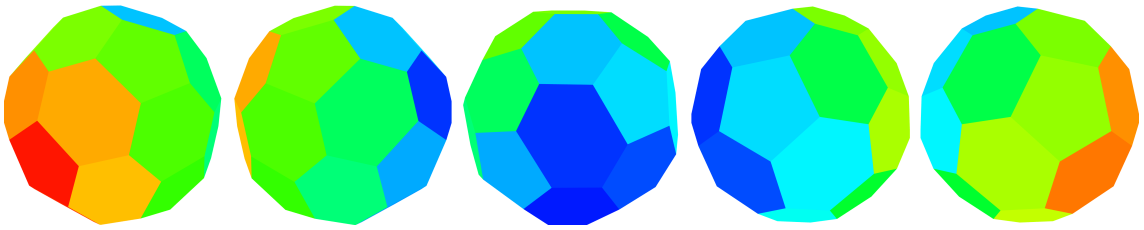

Figure 8: Coloured 3D model of the detector sphere, camera position is 45 ° above the equator. From left to right, the camera has been rotated by −120 °, −60 °, 0 ° (centre: module 2 focussed, one segment above module 1, the beam entrance), +60 °, and +120 °.

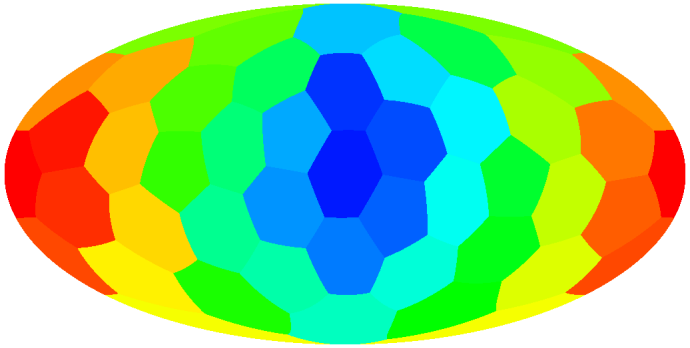

Figure 9: Mollweide projection of the setup. The colours correspond to those in Fig. 8.

projections usually found in cartography tend to be size accurate, yet this is no inherent property. The Robinson projection employs a table of data values unlike the Hammer projection which can be expressed as a mathematical formula. However, inspired by the data visualisation of WMAP measurements [5], the Mollweide projection was chosen instead. This transformation is size accurate, thus enabling a second visualisation beside the ubiquitous two-dimensional graphs.

The positions of the modules within the array's polygonal, near-spherical geometry are presented both as a 3D rendering (Fig. 8) and a Mollweide projection (Fig. 9). In these illustrations, equal colours indicate the same module number.

For subsequent plots, pseudo-colours were used to indicate high (red) and low (blue) values.

4.2 α background

Without any external source, the pulse-height spectrum is dominated by α decay within the scintillator crystals. As the α decay depends on the amount of impurities

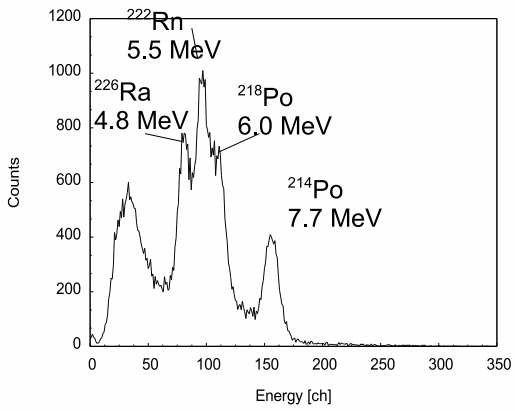

Figure 10: α spectrum from module 23, resolution of 10.8 % at 7.7 MeV.

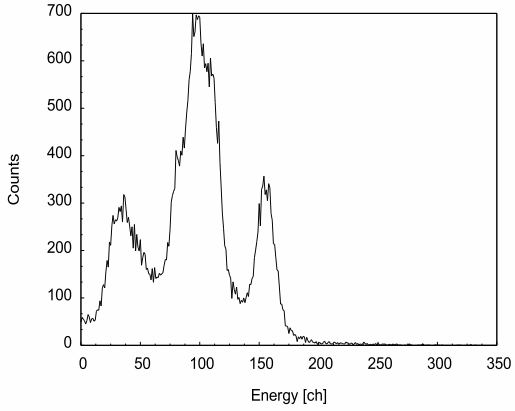

Figure 11: α spectrum from module 15, resolution of 11.5 % at 7.7 MeV.

within the crystal, the background and the possible resolution necessarily vary from module to module.

The best spectrum was obtained from module 23 (Fig. 10), where the α peaks caused by the various decays are well separated. This is also reflected by the calculated resolution of $\frac{\mathrm{FWHM}(7.7\,\mathrm{MeV})}{7.7\,\mathrm{MeV}} = 10.8\,\%$. Unfortunately, most modules showed an α spectrum more akin to the one in Fig. 11; the three peaks around 5.5 MeV cannot be distinguished anymore.

Moreover, module 3 did not return any signal at all, so even though the majority of the modules arrived in Frankfurt are working properly, some did not. In order to verify that this failure was not due to the voltage divider, the latter was exchanged. However, the problem persisted.

Comparing the count rates of all modules, module 32 was identified (cf. Fig. 12) as measuring an exceptionally high background. Without any further testing, two possible reasons for this irregularity are suggested: either the crystal was siginificantly contaminated by radium or it was malfunctioning.

4.3 Energy measurements

4.3.1 Resolution

In order to distinguish between bad resolution and low amount of Ra impurities that both may cause inseparable peaks around 5.5 MeV (see Fig. 11), two (external) radioactive sources were employed. For this purpose, ^{137}Cs with its peak at 0.662 MeV and ^{60}Co with its prominent lines at 1.17 MeV and 1.332 MeV as well as a bump at

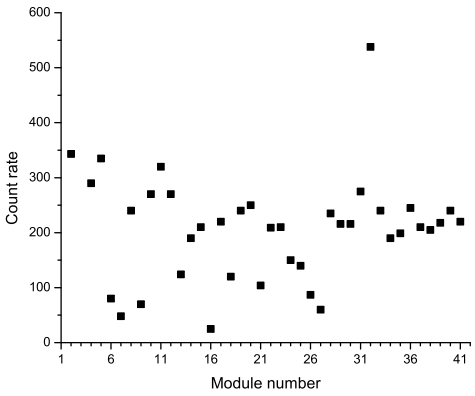

Figure 12: Background count rates as a function of the module number.

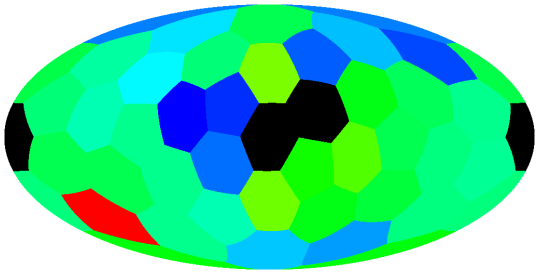

Figure 13: Angular distribution of the data given in Fig. 12.

the sum energy of both peaks (2.52 MeV) were used. The special property of the latter having two lines being relatively close together permitted immediate visual estimation of the energy resolution without requiring a Gaussian fit. Acquiring data for at least 10 minutes ensured that sufficient statistics were collected.

Having a very good energy resolution, module 2 was used as a reference for the peak positions in subsequently acquired pulse-height spectra of the other modules (Fig. 14). Located within a small box, the sources were sticked in front of the crystal under investigation (every crystal was measured on its own). In the course of this measurement, two more modules – no 21 and no 31 (Figs. 16 and 17, respectively) – which had previously remained unsuspicious, exhibited γ spectra that did not show any similarities to those of the other segments. Swapping the voltage dividers did not improve the signal, so the modules have to be considered malfunctioning.

Comparing the count rates measured with the γ sources in place (Fig. 18) to the α measurements (Fig. 12), module 32 does give a sensible value. Looking at its spectrum (Fig. 15) does not yield any exceptional features, so the discrepancy in the α measurements is probably due to a high amount of Ra impurities compared to the other modules.

4.3.2 Calibration

With the known energy of the ^{137}Cs and ^{60}Co peaks, it was possible to calibrate the pulse-height spectrum. The module proved to have good linearity (cf. Fig. 20) even after gathering pulses for just ten minutes. Subsequent tests with module 23 having

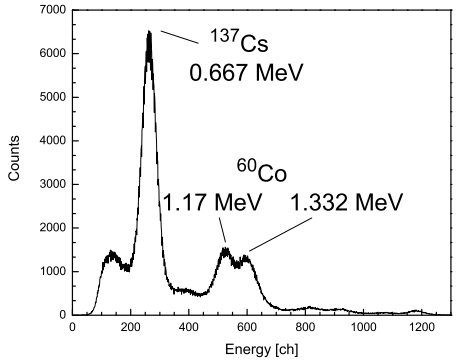

Figure 14: Pulse-height spectrum of module 2 with very good resolution, showing clearly distinguishable lines of ^{60}Co at 1.17 MeV and 1.332 MeV and the ^{137}Cs line ($\frac{\Delta E}{E}$ at 0.662 MeV: 25.3 %).

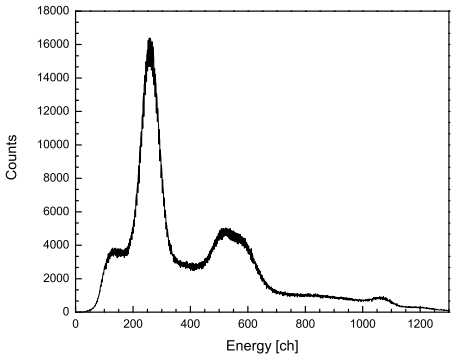

Figure 15: Module 32 exhibiting a mediocre spectrum; no malfunction can be diagnosed ($\frac{\Delta E}{E}$ at 0.662 MeV: 34.2 %).

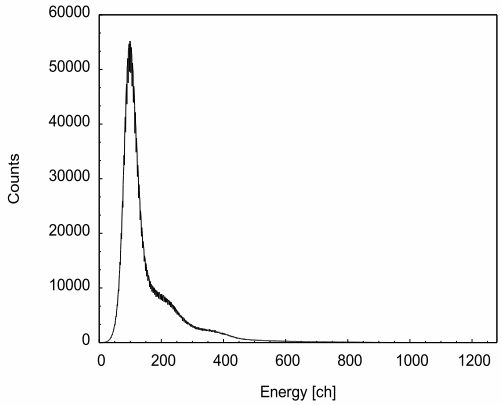

Figure 16: γ spectrum of module 21, lines of ^{60}Co are missing (compare to Fig. 14), so the peak is probably not caused by ^{137}Cs γ emission.

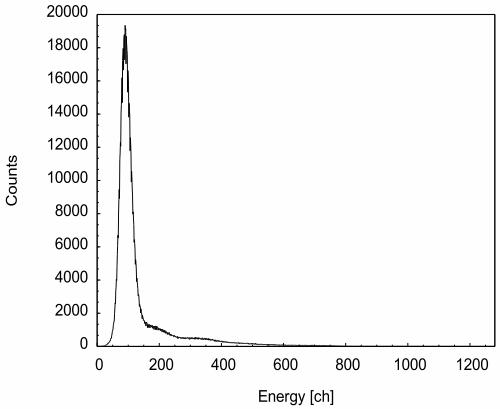

Figure 17: Spectrum of module 31, showing similar problems as module 21 (Fig.16).

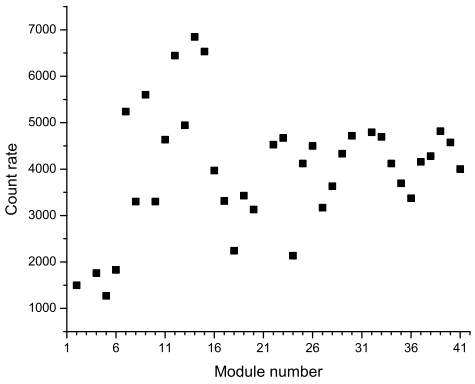

Figure 18: γ count rates as a function of the module number.

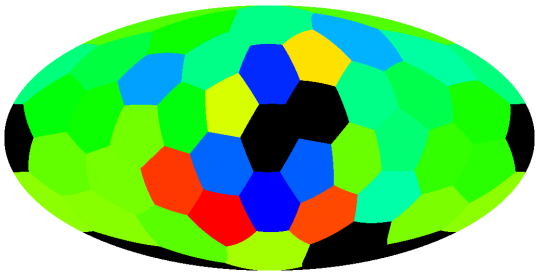

Figure 19: Angular distribution of the data given in Fig. 18.

an even better resolution than no 2 showed that data acquisition runs of one hour improve the linearity due to better statistics (compare Figs. 21 to 22).

4.3.3 Comparison

Comparing the resolution nowadays with the measurements shortly after the time of building, differences between first operation and the current status of the detector become visible (compare Figs. 23 and 24). For low energies, the resolution has degraded by a factor of two – however, at higher energies it seems to have been quite stable if not slightly improved. While not mentioned explicitly, the reference diagram taken from [20] is supposed to have been improved using particle discrimination. As explained above, this has not been implemented yet and may lead to the described discrepancies. Furthermore, the optical connection between the scintillator and the photomultiplier (see section 2.2.2) experiences a significant process of aging [20, p. 606] that might also be connected to the observed degradation. For this reason, the exchange of the silicon oil is suggested, preferably for all modules. As removing the old oil is a difficult task, it will probably be better to start with the modules that show an invalid or no signal (no 3, no 21, and no 31, see above).

The aging process of the silicon oil can be observed first by a decreasing pulse height of the fast component. Therefore, it was suggested to check the fast-to-slow-component ratio as a very good indicator for the necessity to swap the oil. However, this fact was not explored in the present work.

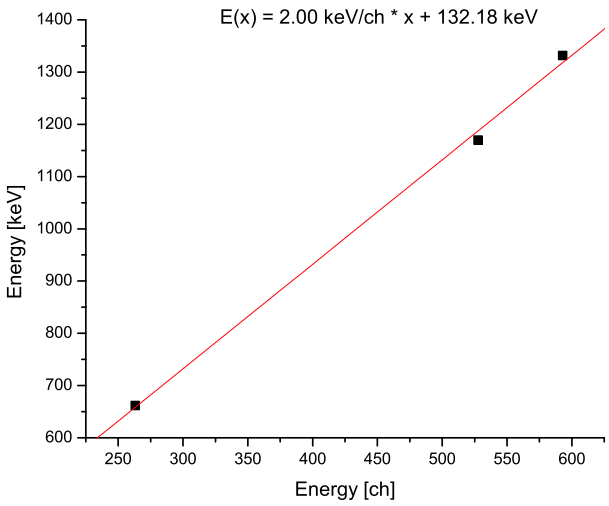

Figure 20: Energy calibration of module 2; no data for 2.5 MeV was used as the bump is hardly visible (see Fig. 14)

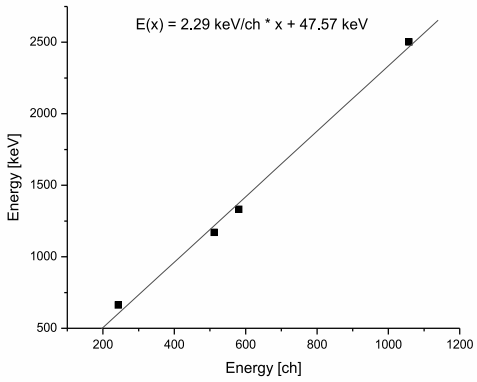

Figure 21: Energy calibration of module 23 resulting from a measurement that ran for 10 minutes

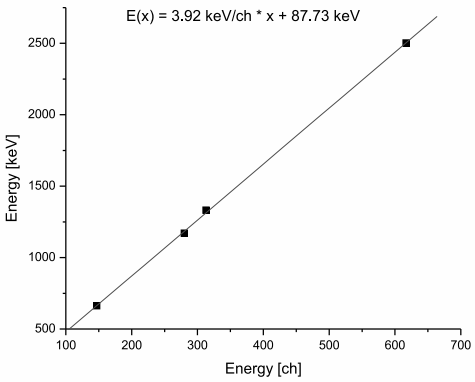

Figure 22: Energy calibration of module 23 after acquiring data for 1 hour; an improvement of linearity in comparison to Fig. 21 is immediately visible

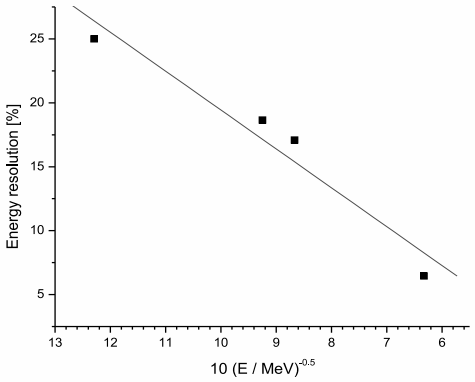

Figure 23: Energy resolution of the best module (no 23)

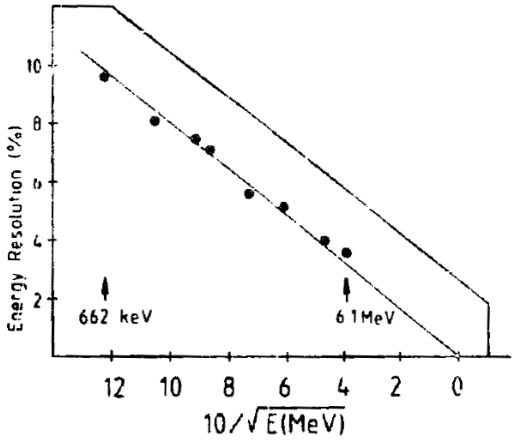

Figure 24: Energy resolution of the best detector module at the time of array construction (diagram taken from [20, p. 605])

4.4 Timing measurements

4.4.1 Resolution

For time resolution measurements, the ^{60}Co source was used since there are two photons emitted simultaneously. Considering the optimal case, one photon is detected within the reference module – again, no 2 was used – while the other γ quantum is detected in the module under inspection. It triggers a stopping signal after which the flash ADC searches its ring buffer backwards in order to find the starting signal from the reference module in a second channel. In this mode, the channel number corresponds to the time difference between the two signals. For each module, a run time of approximately 4 minutes was scheduled half of which the delay was in use.

Calibrating the obtained spectrum was done by extending the wire from the module in question using a cable that delayed the signal by 10 ns. Therefore, a second peak appeared at a different position with the difference in channels corresponding to the aforementioned delay time. For better statistics, a one hour run was performed exemplarily for module 23 yielding an average resolution ($\frac{1}{2}\left(\frac{\Delta t_1}{t_1} + \frac{\Delta t_2}{t_2}\right)$) of 541 ps (compare Fig. 25).

4.4.2 Comparison

A summary of the time resolution from the different crystals is given in Fig. 26. Comparing the time of building the detector to the current status, the degradation

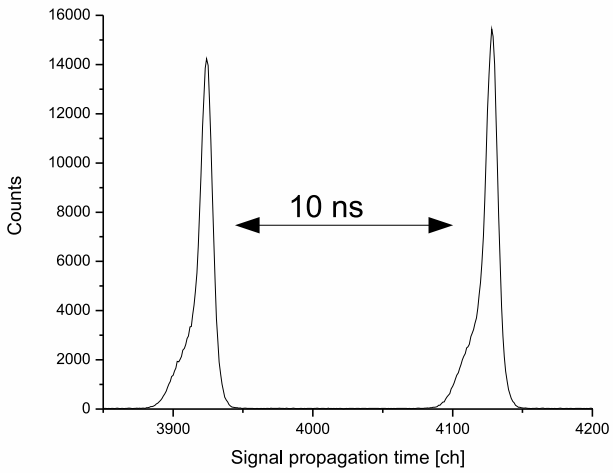

Figure 25: Time resolution measurement for module 23 yielding an average resolution of 541 ps.

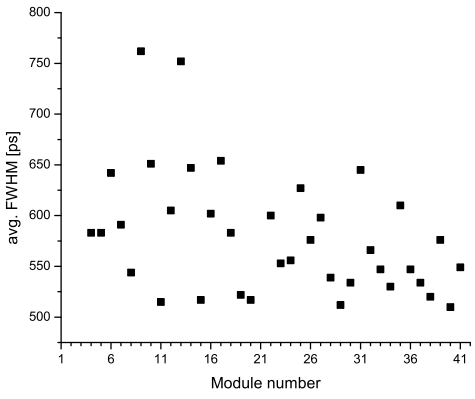

Figure 26: Summary of the time resolution.

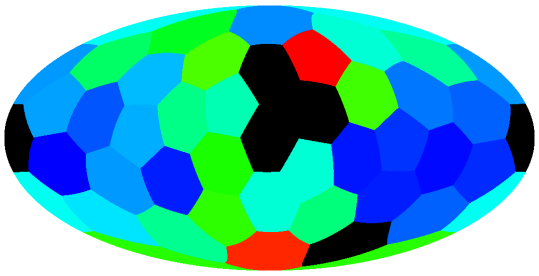

Figure 27: Angular distribution of the data given in Fig. 26.

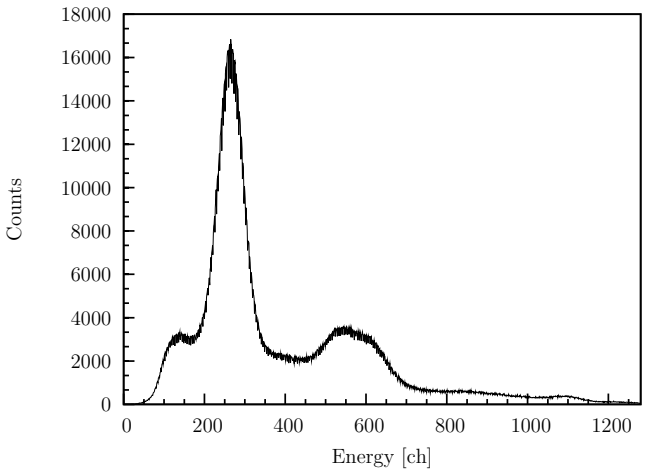

Figure 28: Energy resolution of module 40, the best module in time measurements. The best energy resolution of a single module is given in Fig. 14.

of the resolution becomes visible: At the time of building the detector, a "time resolution [of] 500 ps" was advertised ([20, p. 595]); today, even the best modules only achieve a resolution of approximately 510 ps ranging up to 750 ps for the worst crystal.

From the collected results, it was impossible to find any correlation between good time and energy resolution. On the one hand, modules with good energy resolution (for example no 2) may show a mediocre time resolution. On the other hand, module 40 exhibiting the best time resolution does not perform very well in energy measurements (compare Figs. 28 and 14).

5 Conclusion

Speaking in general, the transfer from Karlsruhe to Frankfurt was a success. The majority of the modules have been proven to function correctly, only three modules are working improperly and of these, only one, module 3, does not give any signal. Assessing these segments as problematic was a very important part of this thesis as it provides a starting point for further improvements. It is suggested that changing the silicon oil for module 3 might remedy the situation; if not, a replacement photomultiplier tube might still be stored in Karlsruhe. If the module still seems to be broken, it is possible to swap the most expensive part of the module, the BaF_2 crystal, for which a spare part exists as well.

A similar diagnosis will be required for the other two defective modules, but it may be possible that substituting the silicon oil is sufficient. However, this procedure is not easy as any old oil glues the fragile photomultiplier tube to the brittle scintillator crystal. Gently contorting the tube helps to separate the parts, yet this course of action requires patience.

It will be interesting to note, whether the repaired modules will exceed the resolution measured for most of the modules. The tendency of the time resolution achieved during the first tests of the detector in the 1980s has been reproduced even though the aging process of the optical connection or possibly other aspects lower the signal quality. The restoration of module 3 might give insights on how much room there is for overall improvement when only considering the detector modules.

Current results and original data

At the moment, the discrepancy between the current resolution and the original data may be explained by the following facts:

Firstly, the current setup does not employ any particle discrimination. Natural radioactivity and noise generated by the decay chains within the BaF_2 may reduce the signal quality.

Secondly, the condition of the silicon oil is unknown, it is unclear at what time the last replacement was conducted. Its aging process affects resolution measurements as was noted in Karlsruhe (see [20, p. 607]). Analysis of the fast-to-slow-component ratio may give hints on which modules need to go through the procedure of substituting the silicon oil.

Thirdly,the results from the first days of the detector were reproduced with a different set of electronics. While in the 1980s an elaborated and complicated system of analog devices was used to improve and record the data, the measurements presented in this thesis employed only a flash ADC and no further data cleanup. Therefore, there is probably room for improvement once the possibilities of the software are used to a greater extent.

Exploring its capabilities, the detector array will provide cross-section data that will help improve current ideas about nucleosynthesis and even the universe as a whole. However, its segmentation into modules allows testing interesting aspects, for example significant anisotropies during the capture process should be notable. After a vignetting procedure, differences from a uniform distribution should become obvious. Of course, the angular resolution will be low: $\frac{4\pi}{42} \approx 300\,\text{mrad}$ – the WMAP mission mentioned above aims at a resolution of $0.23° \mathrel{\hat{=}} 5\,\text{mrad}$ (cf. [1]). Using the Mollweide projection to visualise the recorded data should show a correlation between the sample shape and its emission or scattering characteristics – this will be especially interesting, if the geometry does not imply a homogenous distribution.

Acknowledgements

I would like to thank Prof. Dr. U. Ratzinger for supporting this work and providing me with a way to obtain my bachelor's degree.

Of course, without the support from Dr. F. Käppeler, who is an expert on this detector and who provided me with lots of feedback, this work would not have been possible.

Dr. M. Heil, Dr. R. Plag, and Dr. R. Reifarth were always available for any questions arising about the detector and its operation and hinted me at possible problems, for which I am very grateful.

N. Vasilev, with whom I have collaborated closely, has provided assistance in numerous ways; he was always open to discussions and questions and was always aware of what might be done next.

Finally, I appreciate the support from the colleagues of my working group, namely L.-P. Chau, Dr. M. Droba, N. Joshi, Dr. O. Meusel, P. Nonn, K. Schulte, and C. Wiesner, as well as everyone else not listed by name who helped me complete this work.

References

[1] WMAP Angular Resolution. NASA website, http://map.gsfc.nasa.gov/mission/observatory_res.html, retrieved on July 14, 2008.

[2] E. Altstadt, C. Beckert, R. Beyer, H. Freiesleben, V. Galindo, M. Greschner, E. Grosse, A. R. Junghans, J. Klug, D. Légrády, B. Naumann, K. Noack, K. Schilling, R. Schlenk, S. Schneider, K. Seidel, A. Wagner, and F.-P. Weiss. nELBE: Neutron time-of-flight experiments at ELBE, Aug. 27, 2007.

[3] C. Arlandini, M. Heil, F. Käppeler, R. Reifarth, F. Voss, and K. Wisshak. Sternmodelle im Test: Die Phase der Roten Riesen. *Forschungszentrum-Nachrichten 2/2001*, pages 177–188.

[4] H. Beer, S. Dababneh, M. Heil, F. Käppeler, R. Plag, W. Rapp, R. Reifarth, F. Voss, and K. Wisshak. Laborbestimmung stellarer Neutronenreaktionen. *Forschungszentrum-Nachrichten 2/2001*, pages 189–200.

[5] C. L. Bennett, M. Halpern, G. Hinshaw, N. Jarosik, A. Kogut, M. Limon, S. S. Meyer, L. Page, D. N. Spergel, G. S. Tucker, E. Wollack, E. L. Wright, C. Barnes, M. R. Greason, R. S. Hill, E. Komatsu, M. R. Nolta, N. Odegard, H. V. Peirs, L. Verde, and J. L. Weiland. First year Wilkinson Microwave Anisotropy Probe (WMAP) observations: Preliminary maps and basic results. *The Astrophysical Journal*, 148, 2003.

[6] H. H. Binder. *Lexikon der chemischen Elemente*. S. Hirzel Verlag, 1999.

[7] W. L. Freedman et al. Final Results from the Hubble Space Telescope Key Project to Measure the Hubble Constant. *The Astrophysical Journal*, 553:47–72, 2001.

[8] F. Gunsing et al. Neutron capture measurements at the CERN-n_TOF facility for ADS applications. *Proceedings of the 11th International Symposium Capture Gamma-ray Spectroscopy and Related Topics*, Sept. 2–6, 2002.

[9] M. Heil. Neutron capture measurements (NCap), Nov. 9, 2004.

[10] E. Hubble. A relation between distance and radial velocity among extra-galactic nebulae. *Proceedings of the National Academy of Sciences of the United States of America*, 15(3):168–173, 1929.

[11] Y. Kadi and J.-P. Revol. Design of an accelerator-driven system for the destruction of nuclear waste. *Workshop on Hybrid Nuclear Systems for Energy Production, Utilisation of Actinides & Transmutation of Long-Lived Radioactive Waste*, pages 91–92, Sept. 4–7, 2002.

[12] K. Kleinknecht. *Detektoren für Teilchenstrahlung*. Teubner, Wiesbaden, 4th and revised edition, 2005.

[13] I. M. McHardy, G. C. Stewart, A. C. Edge, B. Cooke, K. Yamashita, and I. Hatsukade. GINGA observations of Abell 2281 – Implications for H_0. *Monthly Notices of the Royal Astronomical Society*, 242:215–220, Jan. 1990.

[14] A. Mengoni and the n_TOF Collaboration. Astrophysics program at the CERN n_TOF facility. *Proceedings of an International Symposium on Astrophysics, Symmetries, and Applied Physics at Spallation Neutron Sources*, 2002.

[15] R. Reifarth. *Die Verzweigung des Nukleosynthesepfades am ^{128}I – ein stellares Thermometer*. PhD thesis, Eberhard-Karls-Universität, Tübingen, 2002.

[16] R. Reifarth, R. Haight, M. Heil, F. Käppeler, and D. Vieira. Neutron capture measurements at a RIA-type facility. *Nuclear Instruments and Methods in Physics Research A*, 524:215–226, 2004.

[17] J. P. Snyder. Map projections: A working manual. 1987.

[18] W. H. Tait. *Radiation Detection*. Butterworth, London, 1980.

[19] A. Unsöld and B. Baschek. *Der Neue Kosmos*. Springer, Berlin, 7th edition, 2004.

[20] K. Wisshak, K. Guber, F. Käppeler, J. Krisch, H. Müller, G. Rupp, and F. Voss. The Karlsruhe 4π barium fluoride detector. *Nuclear Instruments and Methods in Physics Research A*, 292:595–618, July 1990.

Eidesstattliche Erklärung

Ich versichere hiermit, dass ich die vorliegende Arbeit selbständig verfasst, keine anderen als die angegebenen Hilfsmittel verwendet und sämtliche Stellen, die benutzten Werken im Wortlaut oder dem Sinne nach entnommen sind, mit Quellen- bzw. Herkunftsangaben kenntlich gemacht habe.

Frankfurt, den 1. September 2008

Stefan Schmidt